Selection of suitable operating conditions for planar anode-supported direct-internal-reforming solid-oxide fuel cell

Suranat Wongchanapai*, Hiroshi Iwai, Motohiro Saito, Hideo Yoshida

Department of Aeronautics and Astronautics, Kyoto University, Yoshida Honmachi, Sakyo-ku, Kyoto 606-8501, Japan

ARTICLE INFO

ABSTRACT

A numerical model was implemented to analyze the thermodynamic performance of the co- and counter-flow operations of an anode-supported direct internal reforming (DIR) planar solid oxide fuel cell (SOFC). This developed model was validated by comparing with experimental and simulated results taken from the literature. The model is capable of capturing the detailed distribution of the local temperatures, species concentrations, current density, and polarization losses in streamwise direction. Energy and exergy concepts were used to evaluate the DIR-SOFC performance under co- and counter-flow operations. The study indicates the energy and exergy efficiencies of DIR-SOFC performance under co-flow operation are more sensitive to the increase of current density than that under counter-flow operation. Particular attention was paid to cell temperature profiles to avoid mechanical failure due to high thermal stresses. The result shows that the material constraints need to be considered as well as the energy and rational efficiencies in evaluating the performance of SOFC. The preferred flow configuration can be changed depending on the cell geometry and operation conditions if we consider the material constraints.

© 2011 Elsevier B.V. All rights reserved.

1. Introduction

Among fuel cells, high operating temperature SOFCs could improve and promote the exploitation of power generation system as combined heat and power systems to raise the energetic efficiency [1–7]. Furthermore, high operating temperature SOFCs also offer many advantages over other fuel cells (i.e., fuel flexibility, tolerance to impurities). However, this high operating temperature poses a problem in terms of the thermal management of SOFCs [8]. Because SOFCs are made of fragile ceramic materials, a large temperature gradient may cause cracking of the cell. It is required to properly control the cell temperature distribution for its safe and efficient operation.

One of the attracting features of SOFC is the direct internal reforming (DIR) of hydrocarbon fuels. The endothermic reforming reaction proceeds on the Ni catalyst in the anode in the direct internal reforming process. It utilizes the waste heat generated by the electrochemical reaction and other irreversible processes to offset the heat requirements of the reforming reaction, resulting in the increase in the performance of the SOFC. It also reduces the amount of the extra air supplied to the cathode channel because the cooling demand is reduced, thus lowering the cost. One drawback is that it may cause a large temperature gradient to the cell because

of the strong endothermic nature of the reforming reaction. However, direct measurements of the temperature distribution in an operating DIR-SOFC are difficult because of the high temperature, narrow channel gaps, and small flow rates.

Numerical simulation is expected to be an effective tool to understand the phenomena in a DIR-SOFC system. CFD-based two- and three-dimensional simulations of fuel cells can be found in the literature [9–11] but owing to the heavy computational load, the computational domain is generally limited to a single module or channel. Iwai et al. [12] recently developed a CFD based quasi-three-dimensional simulation model that applies the volume-averaging method to the flow passages by assuming that a porous material is inserted as a current collector. It reduces the computational time and cost while maintaining the ability to solve the flow and pressure fields in the SOFC. The CFD based simulation is effective to investigate detailed phenomena in the SOFC but it is an expensive computational process for a system level analysis where modules are usually described with lumped (0-dimensional) models. The use of the lumped model to DIR-SOFC, however, needs to be carefully examined before its application to a system analysis because the large temperature gradient expected in a DIR-SOFC and its effects cannot be taken into account if a lumped model is used. To consider the distributions of variables in the DIR-SOFC, 1-D model is at least needed.

Campanari [13] proposed two-dimensional CFD based numerical models for electrolyte-supported DIR-SOFC. They performed parametric analysis on the effects of heat losses, air ratio and cell

* Corresponding author. Tel.: +81 75 753 5203; fax: +81 75 753 5203.
 E-mail address: suranat.w@hs8.ecs.kyoto-u.ac.jp (S. Wongchanapai).

Nomenclature

A	cell active area, m^2
A_c	cross section area, m^2
A_s	surface area, m^2
C_p	specific heat at constant pressure, J kg^{-1} K
$D_{i,eff}$	effective diffusivities of the species i, m^2 s^{-1}
D_{im}	diffusivity of the species i, m^2 s^{-1}
D_{ik}	Knudsen diffusion of the species i, m^2 s^{-1}
d_h	channel hydraulic diameter, m
d_{pore}	pore diameter, μm
ex	specific exergy flow, J kg^{-1}
E_{CH_4}	activation energy of the methane reforming reaction
Ex	exergy flow rate, W
F	faraday constant, 96487 C mol^{-1}
h	convective heat transfer coefficient, W m^{-2} K
i_c	current density, A m^{-2}
i_0	exchange current density, A m^{-2}
k_{shift}	rate constant of forward shift reaction, mol m^{-3} Pa^2 s
K	permeability, m^2
K_p	equilibrium constants
m	mass flow, kg s^{-1}
M_i	molecular weight of species i, kg mol^{-1}
n_e	number of electrons participating in the electrochemical reaction
n_i	mole flow rate of species i, mol s^{-1}
P	pressure, Pa
P_{elec}	electrical power, W
p_i	partial pressure of species i, Pa
Q	heat generation rate, W m^{-3}
R_{reform}	reforming reaction rate, mol m^{-3} s
R_{shift}	shift reaction rate, mol m^{-3} s
R	universal gas constant, 8.314 J mol^{-1} K
T	temperature, K
V	electric potential, V
V_{OC}	open-circuit voltage, V

Greek letters

ΔG°	change of standard Gibbs free energy, J mol^{-1}
ΔH	enthalpy change, J mol^{-1}
ε_p	porosity
η	energetic efficiency
η_{act}	acticvation polarization loss, V
η_{conc}	concentration polarization loss, V
η_{ohm}	ohmic polarization loss, V
λ	thermal conductivity, W m^{-1} K
ρ_{air}	air stream density, kg m^{-3}
ρ_{fuel}	fuel stream density, kg m^{-3}
ρ_j	specific electrical resistance of the component j, Ω m^2
σ	ionic/electronic conductivity, S m^{-1}
δ	thickness, m
τ	tortuosity
ψ	rational efficiency

Subscripts

0	properties of the environment
air	air, air channel
an	anode
ca	cathode
ch	chemical
co-flow	co-flow cell configuration
counter-flow	counter-flow cell configuration
fuel	gas mixture at the fuel channel, fuel channel
H$_2$	hydrogen oxidation
in	inlet value
out	outlet value
PEN	positive-electrolyte-negative structure
ph	physical
shift	shift reaction
SOFC	fuel cell
SR	steam reforming
TPB	three-phase boundary.

configurations (cross-, co- and counter-flow cells) on the temperature distributions of a planar electrolyte-supported DIR-SOFC. To improve power output, an anode-supported planer DIR-SOFC recently gains more attentions. Aguiar et al. [14] and Li et al. [15] developed one-dimensional model of an anode-supported planer DIR-SOFC and applied it to the co- and counter-flow operations. Both reported the detailed distributions of the cell temperature, species more fractions, current density and electrochemical performance. Ho et al. [16] performed CFD-based three-dimensional simulations using a commercial package (Star-CD) and reported similar results. All these studies [14–16] agree that the counter-flow configuration has advantages with high performance compared to the co-flow configuration. However, an unfavourable steep temperature gradient is also commonly predicted for the counter-flow configuration. Ho et al. reported that a decrease of the air inlet temperature alleviated the large temperature gradients in the counter-flow case but it inevitably decreases the cell average temperature and thus lowers the cell efficiency. In a DIR-SOFC where a non-uniform temperature distribution is expected, the selection of the configurations and operation conditions need to be done considering not only the efficiency but the material constraints.

In this paper, we develop a numerical model of an anode-supported planer DIR-SOFC to clarify suitable operating parameters for co- and counter-flow operations considering both the efficiency and material constraints. With its future application to a system analysis in mind, the model is one-dimensional and capable of performing exergy analysis. A comparative performance study between co- and counter-flow planar anode-supported DIR-SOFCs is performed under constant fuel and air utilization factors with the distribution of the temperatures, species concentrations, current density, and polarization losses. Since changing inlet temperatures can have either a beneficial or an undesirable impact on performance and life span of the cell, effects of the current density and inlet temperatures under co- and counter-flow operations are investigated by energy and exergy methods to clarify the maximum cell performance with lowest risk of thermal failure. The previous studies in this category found in literature report the advantage of a counter-flow configuration over a co-flow configuration from the energy efficiency point of view [14–16]. In this study we revisit the discussion on the preferred flow configuration with consideration of the material constraints as well as the energy and exergy efficiencies.

2. Model description

2.1. Computational domain

In a practical planer SOFC system, a number of cells are stacked in series. When the number of the stacked cells is sufficiently large, most of the cells located in the core of the stack are similarly surrounded by other cells and are therefore operated in a similar
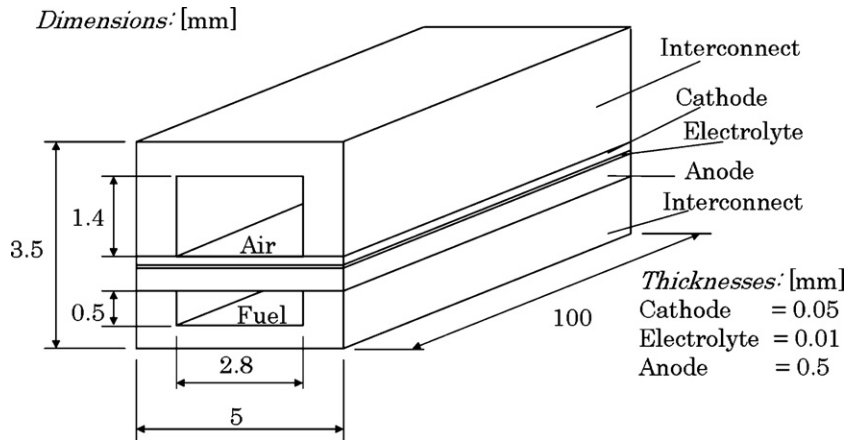
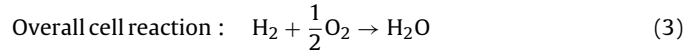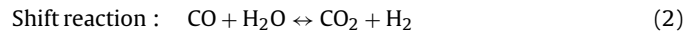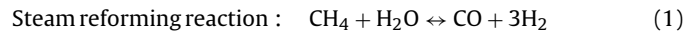**Fig. 1.** Schematic of one channel region and its geometries.

situation to each other. Attention is therefore focused in this study to a single cell in such a situation in a stack assuming that it represents the entire stack characteristics. In other words, we assume an ideal thermal insulation of the system and the cells in the stack are identical. As shown in Fig. 1, a planar SOFC of co- and counter-flow types was modeled with the pair of two channels under a steady-state condition; the SOFC is composed of the fuel and air channels, the PEN structure (anode, electrolyte and cathode) and interconnection. As shown in Fig. 2, heat loss near the edge of the cell stack is also neglected.

The electrochemical reaction is considered to be attributed to only hydrogen; the electrochemical fuel value of CO is readily exchanged for hydrogen by the rapid shift reaction assuming chemical equilibrium [17]. In other words, CO is considered to take part only in the shift reaction. Whereas the open-circuit voltage (V_{OC}) of an internal reforming SOFC is calculated according to the electrochemical oxidation of H_2, the species' consumption and production is determined collectively from the steam reforming reaction and shift reaction.

As presented in Fig. 2, the one channel region is discretized into 90 control volumes of uniform size (ΔX) in the x-direction. Each control volume contains three temperatures corresponding to air and fuel streams, T_{fuel} and T_{air}, and temperature of the cell or the solid part (PEN and interconnect are lumped together), T_{solid}, respectively. The mass and heat balances of each control volume are analyzed and solved by finite difference method. Fig. 2 also shows that the fuel always flows in the x-direction while air flows either in the x-direction (co-flow operation) or in the negative x-direction (counter-flow operation).

2.2. Mass balances

Mass balances are formulated for each species on the basis of the relationship between the local current and the change in the concentrations. The following three equations summarizes the reactions considered in the cell.

Steam reforming reaction : $\quad CH_4 + H_2O \leftrightarrow CO + 3H_2$ (1)

Shift reaction : $\quad CO + H_2O \leftrightarrow CO_2 + H_2$ (2)

Overall cell reaction : $\quad H_2 + \dfrac{1}{2}O_2 \rightarrow H_2O$ (3)

The open-circuit voltage (V_{OC}), is described by the Nernst equation as a function of operating temperature (T) and partial pressure (p).

$$V_{OC} = \frac{\Delta G^\circ}{2F} + \frac{RT}{2F} \cdot \ln\left(\frac{p_{H_2} \cdot p_{O_2}^{1/2}}{p_{H_2O}}\right) \quad (4)$$

These reactions lead to five mass balances over the unit cell where $\bar{x}$, $\bar{y}$ and $\bar{z}$ are the conversion rates of CH_4, CO and H_2, respectively.

$$\Delta n_{CH_4} = -\bar{x} \quad (5a)$$

$$\Delta n_{CO} = \bar{x} - \bar{y} \quad (5b)$$

$$\Delta n_{CO_2} = \bar{y} \quad (5c)$$

$$\Delta n_{H_2} = 3\bar{x} + \bar{y} - \bar{z} \quad (5d)$$

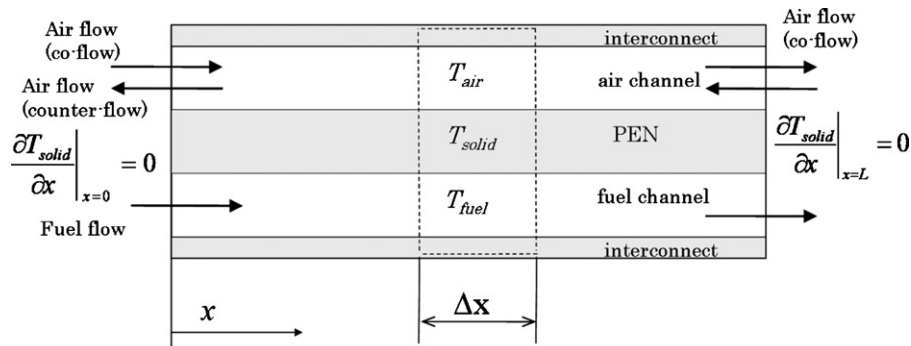$$\Delta n_{H_2O} = -\bar{x} - \bar{y} + \bar{z} \quad (5f)$$

Fig. 2. Discretized domain for co- and counter-flow configuration.

A model proposed by Achenbach [18] is adopted for the reaction rate of the methane reforming reaction:

$$r_{CH_4} = k_{CH_4} p_{CH_4} \ \exp\left(\frac{-E_{CH_4}}{RT}\right) \tag{6}$$

where, E_{CH_4} (= 82 kJ mol^{-1}) is the activation energy of the reaction, k_{CH_4} (= 4274 mol m^{-2}-bar-s) is the pre-exponential factor and p_{CH_4} is the partial pressure of methane.

The chemical equilibrium constant of the shift reaction is another constraint governing relations among chemical components in the control volume.

$$K_{p,shift} = \frac{p_{CO_2} \cdot p_{H_2}}{p_{CO} \cdot p_{H_2O}}$$
$$= \frac{(n_{CO_2} + \bar{y}/n_{tot} + 2\bar{x})(n_{H_2} + 3\bar{x} + \bar{y} - \bar{z}/n_{tot} + 2\bar{x})}{(n_{CO} + \bar{x} - \bar{y}/n_{tot} + 2\bar{x})(n_{H_2O} - \bar{x} - \bar{y} + \bar{z}/n_{tot} + 2\bar{x})} \tag{7}$$

Here, n_i denotes the molar flow rate of species i at the inlet of the control volume. n_{tot} is the total molar flow rate of all chemical components at the same location. If the exit temperature of each control volume is evaluated from energy balance equations described in Section 2.4, chemical equilibrium constant (7) can be obtained and applied to analyze mass conservations of chemical components in each control volume. As mentioned above, the shift reaction is always assumed to be at equilibrium in this study. The equilibrium constant can be given by (8) [19]:

$$K_{p,shift} = \exp(-0.2935Z^3 + 0.6351Z^2 + 4.1788Z + 0.3619) \tag{8}$$

where $Z = (1000/T) - 1$.

2.3. Electrochemical model

2.3.1. Concentration polarization

The concentration polarization is ascribed to the finite gas diffusion processes that govern movement of gasses into and out of the electrochemical reaction site. The potential difference between operations with and without current is the concentration polarization, hence is evaluated as:

$$\eta_{conc,an} = \frac{R \cdot T}{2F} \ \ln\left(\frac{p_{H_2O,TPB} p_{H_2}}{p_{H_2O} p_{H_2,TPB}}\right) \tag{9}$$

$$\eta_{conc,ca} = \frac{R \cdot T}{4F} \ \ln\left(\frac{p_{O_2}}{p_{O_2,TPB}}\right) \tag{10}$$

where the subscript *TPB* denotes the three-phase boundary. To calculate the pressure at the reaction sites, the following equations have been adopted:

$$p_{H_2,TPB} = p_{H_2,an} - i_c \frac{R \cdot T \delta_{an}}{2F \cdot D_{H_2O,eff}} \tag{11}$$

$$p_{H_2O,TPB} = p_{H_2O,an} + i_c \frac{R \cdot T \delta_{an}}{2F \cdot D_{H_2,eff}} \tag{12}$$

$$p_{O_2,TPB} = P_{air} - (P_{air} - p_{O_2,ca}) \exp\left(i_c \frac{R \cdot T \delta_{ca}}{4F \cdot P_{air} \cdot D_{O_2,eff}}\right) \tag{13}$$

In the equations, P represents total pressure, and $D_{i,eff}$ represents the effective diffusivities of the species i at anode and cathode. To evaluate the effective diffusivities, combined ordinary and Knudsen diffusion [20] has been used:

$$\frac{1}{D_{i,eff}} = \left(\frac{\varepsilon_p}{\tau}\right)\left(\frac{1}{D_{im}} + \frac{1}{D_{ik}}\right) \tag{14}$$

Table 1
Calculation based parameters for diffusion overvoltage.

Parameter	Value
Electrode porosity (ε_p)	0.48
Electrode tortuosity (τ)	5.4
Pore diameter (d_{pore}) (μm)	1.0

Taken from [22].

where ε_p and τ are the porosity and tortuosity of electrode materials, respectively, shown in Table 1. Diffusivity of species i in multicomponent gas mixture, D_{im} can be estimated by Wilke [21]:

$$D_{im} = \frac{1 - x_i}{\sum_{j \neq i}(x_j/D_{ij})} \tag{15}$$

where x_i is the mole fraction of gas species i. For prediction of the binary diffusivity of the gas mixture composed of species i and j (D_{ij}), the Fuller–Schettler–Giddings formula [20] is adopted in this study:

$$D_{ij} = \frac{0.1013T^{1.75}((1/M_1) + (1/M_2))^{0.5}}{P\left[\left(\sum \upsilon_1\right)^{1/3} + \left(\sum \upsilon_2\right)^{1/3}\right]^2} \tag{16}$$

where M_i is molecular weight of species i; ($\Sigma \upsilon_i$) represents diffusion volume of species i, which values can be found in [20], Knudsen diffusion (D_{ik}) can be expressed as:

$$D_{ik} = 48.5 d_{pore}\left(\frac{T}{M_i}\right)^{0.5} \tag{17}$$

where d_{pore} is pore diameter.

2.3.2. Activation polarization

Chemical reactions, including electrochemical reactions, involve energy barriers which must be overcome by the reacting species. This energy barrier is called the 'activation energy' and results in activation or charge–transfer polarization, which is due to the transfer of charges between the electronic and the ionic conductors taking place at the three-phase boundary layer of both electrodes. The activation polarization may be regarded as the extra potential necessary to overcome the energy barrier of the rate-determining step of the reaction to a value such that the electrode reaction proceeds at a desired rate. Activation polarization (η_{act}) is normally expressed by the well known Butler Volmer equation.

$$i_c = i_0 \left\{\exp\left(\beta\frac{n_e F \eta_{act}}{RT}\right) - \exp\left[-(1-\beta)\frac{n_e F \eta_{act}}{RT}\right]\right\} \tag{18}$$

The parameters n_e and β in Eq. (18) were set equal to 2 and 0.5, respectively [14]. The activation overpotential can be expressed as

$$\eta_{act} = \frac{2RT}{n_e F} \ \sinh^{-1}\left(\frac{i_c}{2i_0}\right) \tag{19}$$

Table 2
Calculation based parameters for activation overvoltage in Eqs. (20) and (21).

Parameter	Value
Pre-exponential factor for anode (γ_{an}) (A m^{-2})	6.54×10^{11}
Activation energy for anode ($E_{act,an}$) (J mol^{-1})	140,000
Pre-exponential factor for anode (γ_{cat}) (A m^{-2})	2.35×10^{11}
Activation energy for anode ($E_{act,cat}$) (J mol^{-1})	137,000

Taken from [14,23].

Table 3
Specific resistivity for the model.

Component	Material	Specific resistivity (ρ_j) (Ω m)
Electrolyte	YSZ	$2.94 \times 10^{-5} \exp(10,350/T)$[a]
Anode	Ni/YSZ cermet	$2.98 \times 10^{-5} \exp(-1392/T)$[a]
Cathode	LSM-YSZ	$8.114 \times 10^{-5} \exp(600/T)$[a]
Interconnector	Doped LaCrO$_3$	0.0003215[b]

[a] Taken from [1].
[b] Taken from [4].

where i_0 is the exchange current density. Eqs. (20) and (21) are used to evaluate the values of the exchange current density for the anode and the cathode, (see variables in Table 2), respectively.

$$i_{0,an} = \gamma_{an} \left(\frac{RT}{2F} \right) \exp \left(-\frac{E_{act,an}}{RT} \right) \tag{20}$$

$$i_{0,cat} = \gamma_{cat} \left(\frac{RT}{2F} \right) \exp \left(-\frac{E_{act,cat}}{RT} \right) \tag{21}$$

2.3.3. Ohmic loss

The ohmic losses in SOFC are due to: (i) the electrons flow through the anode, cathode and interconnections; (ii) the ionic flow through the electrolyte. The resistivity of the component j (ρ_j) strongly depends on the temperature [5] as presented in Table 3. Using the thickness of the j-th component, δ_j, the total ohmic loss (η_{ohm}) can be expressed as follows:

$$\eta_{ohm} = i_c \sum_j \left(\rho_j \delta_j \right) \tag{22}$$

2.4. Thermal model

The streamwise temperature distributions of the air in air channel, T_{air}, the gas mixture in fuel channel, T_{fuel}, and solid structure, T_{solid}, are considered in the present 1-D numerical simulation. The heat generation and heat transfer processes considered in the model are the heat release and absorption arising from the electrochemical reaction, the electrical resistance, convective heat transfer between the solid phase and gas streams and the conductive heat transfer in solid part. At an elevated temperature, heat transfer by thermal radiation can become important. However it is reported in literature [24–27] that unlike planar electrolyze-supported SOFC or tubular SOFC, the effect of radiation heat transfer on temperature profiles is insignificant in planar anode-supported SOFC and can be negligible. As we only discuss the anode-supported planer SOFC in this study, we neglected the effects of thermal radiation.

Since no heat generation occurs in the airside, the energy conservation equation in air channel is given by:

$$0 = \rho_{air} C_{P,air} \ \Delta x A_{c,air} u_{air} \frac{\partial T_{air}}{\partial x} - h_{air} A_{s,air}(T_{solid} - T_{air}) \tag{23}$$

where ρ_{air} is the density of gas mixture in air channel; $C_{p,air}$ is the specific heat capacity of gas mixture in air channel and $A_{c,air}$ is the cross section area of the channel. The heat transfer coefficient h is given by the Nusselt expression

$$h = \frac{Nu \times \lambda}{d_h} \tag{24}$$

where d_h is the channel hydraulic diameter. The values of Nusselt number and thermal conductivity are set referring literature [28,29] and are summarized in Tables 4 and 5.

For the solid part of the cell, the energy conservation equation is given by:

$$Q_{source,solid} = \lambda_{solid} A_{c,solid} \ \Delta x \frac{\partial^2 T_{solid}}{\partial x^2} + h_{air} A_{s,air}(T_{solid} - T_{air})$$
$$+ h_{fuel} A_{s,fuel}(T_{solid} - T_{fuel}) \tag{25}$$

Table 4
Nusselt number.

	Air side	Fuel side
Nu	4.0	6.2

Taken from [28].

The heat generation in solid structure ($Q_{source,solid}$) is caused by the effect of electrochemical reaction, steam methane reforming reaction and the ohmic loss, and is given by Eq. (26), where ΔH is the change in enthalpy of each reaction.

$$Q_{source,solid} = -\bar{x} \times \Delta H_{SR} - \bar{z} \times T_{solid} \Delta S_{H_2} + i_c A \eta_{ohm} \tag{26}$$

Heat generation associated with the shift reaction occurs in the fuel channel. The governing energy equation for the fuel channel is:

$$0 = \rho_{fuel} C_{P,fuel} \ \Delta x A_{c,fuel} u_{fuel} \frac{\partial T_{fuel}}{\partial x} - h_{fuel} A_{s,fuel}(T_{solid} - T_{fuel})$$
$$- Q_{source,fuel} \tag{27}$$

The heat generation, $Q_{source,fuel}$, in the fuel channel is expressed as follows:

$$Q_{source,fuel} = -\bar{y} \times \Delta H_{shift} \tag{28}$$

2.5. Exergy related to a stream flow

Exergy associated with material stream is equal to the maximum amount of work obtainable when the stream is brought from its initial state to the dead state by processes. Exergy transfer rate associated with material stream can be divided into physical and chemical exergy components. Physical exergy is the work obtainable by taking the substance through reversible processes from its initial state temperature T and pressure P, to the environmental state. It can be calculated with

$$Ex_{ph} = \sum_i n_i[(h - h_0) - T_0 (s - s_0)]_i \tag{29}$$

where n_i represents the mole flow rate of species i, h is the specific enthalpy and s the specific entropy and the properties indicated with the subscript 0 refer to the environmental state.

Chemical exergy is equal to the maximum amount of work obtainable when the substance under consideration is brought from the environmental state, defined by the parameters T_0 and P_0, to the reference state by processes involving heat transfer and exchange of substances only with the environment. The chemical exergy for mixtures can be calculated as follows:

$$Ex_{ch} = \sum_i n_i(\mu_{i,0} - \mu_{i,00}) \tag{30}$$

where $\mu_{i,0}$ is the chemical potential of species i.

2.6. Definitions of efficiencies

In energy conversion processes, the efficiencies can be defined in many ways. In this study we defined two kinds of efficiencies.

Table 5
Thermal conductivity.

	Anode	Cathode	Electrolyte
λ (W m^{-1} K^{-1})	11	6	2.7

Taken from [29].

Table 6
Operating parameters and SOFC channel geometries used in electrochemical model validation [16].

Parameters	Value
Button cell geometries	
Anode thickness (μm)	1000
Cathode thickness (μm)	20
Electrolyte thickness (μm)	8
Fuel/air stream inlet pressure (bar)	1
Cell mean temperature (K)	873–1073
In let gas composition	
Fuel:	97%H_2, 3%H_2O
Air:	21% O_2 and 79% N_2

2.6.1. Energetic efficiency (η)

In any system, energetic efficiency is defined as the ratio between energy in product outputs to the energy in the fuel inputs. It can be applied to SOFC as follows:

$$\eta = \frac{P_{elec}}{\sum_{CH_4, CO, H_2}(m_{fuel} \times LHV)_{in}}. \tag{31}$$

2.6.2. Rational efficiency (ψ)

To give a realistic indicator of the system efficiency by taking exergy of the working fluid at the outlet that is obviously useful in the next component, the rational efficiency or rational exergetic efficiency is applied. The rational efficiency is one form of exergetic efficiencies initially defined by Kotas [30] as a ratio of the desired exergy output to the total exergy input. The rational efficiency can be applied to SOFC as follows:

$$\psi = \frac{P_{elec}}{\sum (Ex_{fuel} + Ex_{air})_{in} - \sum (Ex_{fuel} + Ex_{air})_{out}} \tag{32}$$

2.7. Numerical result validation

To reveal performance limits and defects, numerical modeling has become a valuable tool for design and analysis. For a reliable discussion, it is essential to validate the numerical results. Because the detailed information on experimental results for direct-internal-reforming SOFCs can rarely be found in literature, in this study, the model verification was achieved by comparing the numerical results with the actual case studies and simulation results by Ho et al. [16].

The electrochemical model used in this study was validated by comparing the numerical results with the experimental data of Zhao and Virkar [22]. The operating parameters and cell geometries are summarized in Table 6. As shown in Fig. 3, the predicted results fairly agree with the experimental counterparts. In particular, a good agreement is achieved when the operating temperature is relatively high at 1073 K. It corresponds to the temperature range of the numerical simulations discussed in the following chapter; consequently, the numerical model reliability can be established. The thermal model was also verified comparing the predicted results with the CFD-based simulation results of Ho et al. for the planar anode-supported SOFC with direct CH_4 reformation [16]. The channel geometries and operating conditions are illustrated in Table 7. In spite of the rather simple modeling of the present study compared to the CFD-based 2-D model by Ho et al., the performance predicted by the present 1-D model agrees reasonably well with the results of Ho et al. [16] as summarized in Table 8. Present results show slightly higher temperature deviations compared to those predicted by Ho et al. for co-flow operation and lower temperature deviations for counter-flow operation. This discrepancy between the two simulations is likely ascribed to the different model for the activation overpotential as well as the material properties taken from different sources.
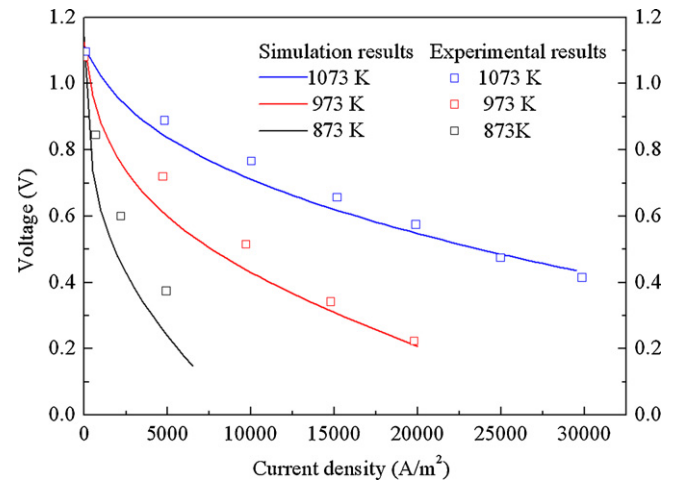
Fig. 3. Comparison of the simulation results with experimental data by Zhao and Virkar [22].

3. Results and discussion

3.1. Fundamental characteristics of DIR-SOFC

The model described in the previous section is applied to a planar DIR-SOFC to find its fundamental characteristics and to confirm the model's capability. Considering the periodic structure, it is modeled with one channel region of a single cell as illustrated in Fig. 1, The cell is a typical anode-supported structure with material properties described in Tables 1–5. The same geometry of one channel region is used for both co- and counter-flow cases. For the sake of consistency and simplicity, the inlet gas composition is chosen as a typical CH_4 syngas composition with steam to carbon ratio of 2 [31]. The fuel flows from left to right in the following figures while the air stream direction is varied corresponding to the co-flow and counter-flow configurations. The fixed operating parameters are summarized in Table 9. Particular attention is paid to temperature profiles of the PEN layer, since the cell stack temperature gradient and maximum local cell temperature are the most important constraints due to material limitations.

3.1.1. Co-flow operation

Strong endothermic reaction of methane reforming proceeds near the inlet. It results in a rapid change of the fuel gas compositions and temperature dip as can be seen in Figs. 4 and 5. The steep

Table 7
Operating parameters and SOFC channel geometries used in model validation [23].

Parameters	Value
Cell length (mm)	100
Cell width (mm)	1
Air channel height (mm)	1
Fuel channel height (mm)	0.6
Anode thickness (μm)	630
Cathode thickness (μm)	50
Electrolyte thickness (μm)	20
Fuel inlet pressure (bar)	1
Air inlet pressure (bar)	1
Fuel utilization rate	0.85
Air utilization rate	0.3
Fuel inlet temperature (K)	1073
Air inlet temperature (K)	1073
In let gas composition	
Fuel:	17.07%CH_4, 2.40%CO, 4.91%CO_2, 26.86%H_2, and 48.75%H_2O
Air:	21%O_2 and 79%N_2

Table 8
Model validation results.

Parameter	Co-flow		Counter-flow	
	Ho et al. [16]	Present	Ho et al. [16]	Present
Voltage (V)	0.7	0.69	0.7	0.73
Power density (W A^{-2})	3850	3819	5320	5747
Current density (i_{ave}) (A m^{-2})				
Average	5500	5498	7600	7888
Maximum	6350	7500	12,400	12,600
Minimum	4000	3400	3500	3216
Cell temperature (T_{solid}) (K)				
Maximum	1155	1184	1260	1160
Minimum	1020	1013	1090	1076

Table 9
Operating conditions for SOFC modeling.

Parameters	Value
Fuel inlet pressure (bar)	1
Air inlet pressure (bar)	1
Fuel utilization rate	0.8
Air utilization rate	0.3
Voltage (V)	0.8
Fuel inlet temperature (K)	1073
Air inlet temperature (K)	1073
Inlet gas composition	
Fuel:	17.10%CH_4, 2.94%CO, 4.36%CO_2, 26.26%H_2 and 49.34%H_2O
Air:	21%O_2 and 79%N_2
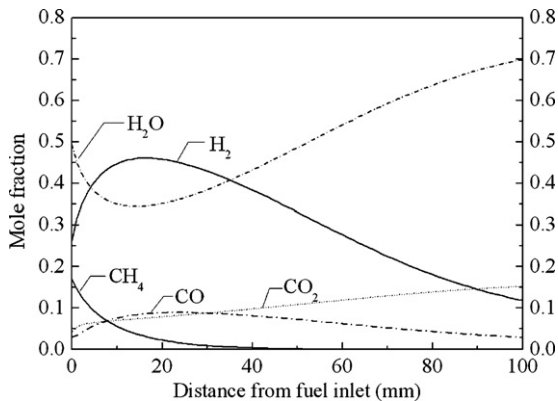
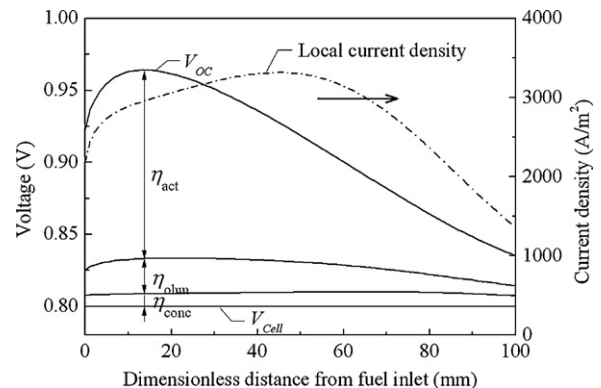**Fig. 4.** Fuel channel mole fractions along the cell length, co-flow operation.

gradients of the methane and steam molar fractions observed in Fig. 4 show their quick consumptions resulting in the prominent increase of the hydrogen molar fraction. Because of the heat consumption associated with the reforming reaction, a local minimum
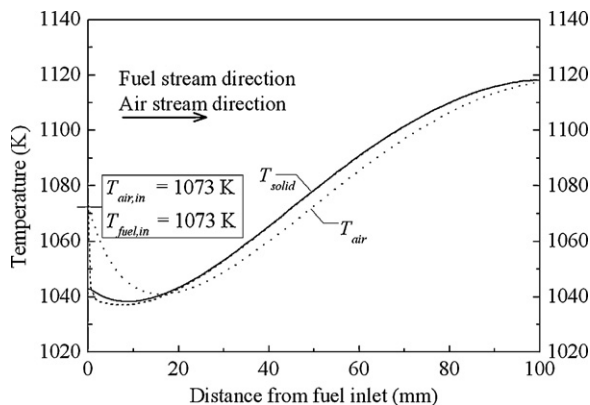
temperature is observed near the fuel inlet as shown in Fig. 5. After methane depleted approximately 47 mm from the fuel inlet, the electrochemical oxidation of H_2 in parallel with the shift reaction are the major reactions proceed in the fuel passage and release reaction heat. It raises the local temperatures of the gasses and the cell resulting in the maximum cell temperature ($T_{solid,max}$) at the end of the channel (1118 K). The maximum cell temperature gradient ($\partial T_{solid}/\partial x)_{max}$ is 1.25 K mm^{-1} observed at the middle of the cell. It is also noted in Fig. 5 that the fuel flow temperature is almost same as the cell temperature because of the small heat capacity of the fuel gas and flow rate. Near the inlet, the air temperature is higher than the fuel temperature. The air flow actually serves as a heat source for the reforming reaction, not as a coolant, in this region under the present condition. The air flow works as a coolant only after $x > 20$ mm where the air temperature is always less than the cell temperature.

Fig. 6 presents the distributions of the open-circuit voltage, polarizations, ohmic loss and local current density under the same operation condition. The average current density was 2779 A m^{-2} in this case. It shows that both the open-circuit voltage and the local current density have maximum values in the middle of the cell but their positions do not coincide. Their distributions are affected by the local temperature and local gas composition. The open-circuit voltage is the highest around $x = 15$ mm where the value of the activation overpotential is also high because of the locally reduced temperature. On the other hand, although the activation overpotential is the lowest near the exit, the open-circuit voltage is also low in this region because most of the fuel (hydrogen) has already been used up. Consequently the electrochemical reaction is most prominent at the middle of the cell. The figure also shows that the activation polarization is the major loss whereas the ohmic loss and the concentration polarization are relatively low and uniform.

Fig. 5. Temperature distributions, co-flow operation.

Fig. 6. Open-circuit voltage, polarization terms and local current density distributions, co-flow operation.

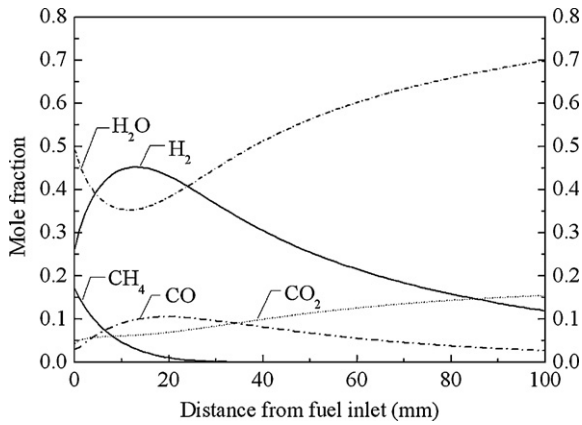Fig. 7. Fuel channel mole fractions along the cell length, counter-flow operation.

Fig. 9. Open-circuit voltage, polarization terms and local current density distributions, counter-flow operation.

3.1.2. Counter-flow operation

Fig. 7 shows the distributions of the mole fractions in the fuel stream for counter-flow case. Comparing Fig. 7 to Fig. 4, it is noted that the reforming reaction proceeds more rapidly in the counter-flow case and methane it is depleted approximately 33 mm from the fuel entrance. This is caused by the elevated cell temperature compared to the co-flow case. The higher the temperature is, the faster the steam reforming proceeds. The main difference between the two cases is the air temperature approaching to the fuel entrance region, $0 < x < 20$ mm, where the reforming reaction is active. While the air flow is directly supplied to the active reforming region in the co-flow case, it goes through the air passage of the cell in the counter-flow case accumulating heat generated in the cell. Consequently, as shown in Fig. 8, the air temperature approaching the active reforming region becomes much higher in the counter-flow case compared to the co-flow case even though the inlet temperatures are the same. This is an effective heat recovery process of a DIR-SOFC. However from the viewpoint of the temperature distribution, the counter-flow configuration needs to be examined carefully. The local cell temperature reaches its maximum value of 1194 K at 30 mm from the fuel entrance and the maximum cell temperature gradient $(\partial T_{solid}/\partial x)_{max}$ is 5.10 K mm^{-1} located at 8 mm from the fuel entrance. Comparing to the co-flow configuration, the maximum local cell temperature is increased 76 K and the maximum cell temperature gradient is increased 8 times. It should be noted that a large temperature gradient causes excessively high stress in the cell resulting in thermal cracking and cell failure. Therefore, the co-flow case is superior to the counter-flow case in term of material point of view and the cell temperature profile must be carefully monitored.
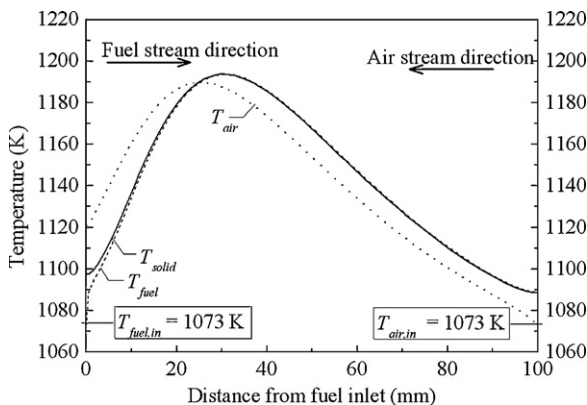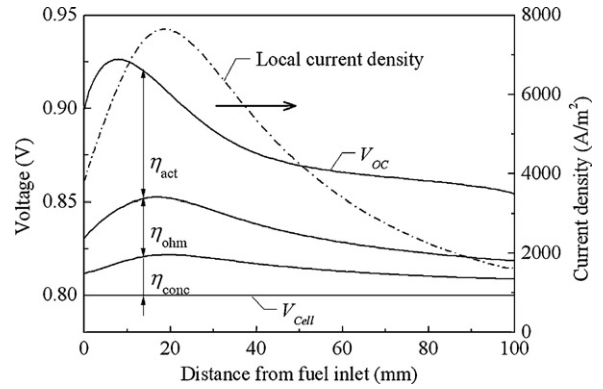
The open-circuit voltage, polarizations, ohmic loss and local current density distributions are shown in Fig. 9. The average current density was 4394 A m^{-2} in this case. The figure shows that the non-uniformity of the local current density distribution is considerably reinforced in the counter-flow configuration compared to that of the co-flow configuration shown in Fig. 6. The ohmic loss and concentration polarization exhibit distributions that track the local current density distribution, whereas raising temperature results in the reduction of activation polarization.

3.2. Effects of current density

To compare the performance of the two configurations, Fig. 10 illustrates the predicted cell efficiencies and power density as a function of current density with cell voltage variation from 0.6 to 0.8 V. All other parameters are fixed at their standard values in Table 9. It can be seen that, the performance of the cell is hindered with an increase of current density. At 1000 A m^{-2}, the power density and efficiencies under the two configurations are very close to each other. The rational efficiency is much higher than energy efficiency, the main exergy losses owing to internal consumptions and the main energy losses associated with waste heat. It shows that there is a considerable potential in SOFC application to generate additional electric or heat power from the outlet streams. As current density increases, the power density difference between co- and counter-flow cases becomes more pronounced. The energetic efficiencies vary from 60.7 to 46.9% and from 61.6 to 54.0%; rational efficiencies vary from 83.8 to 66.1% and from 84.6 to 75.3%, for co-flow and counter-flow cases, respectively. The increase of the difference in the efficiencies between the co- and counter-flow cases is ascribed to the cell temperature difference. Because the fuel

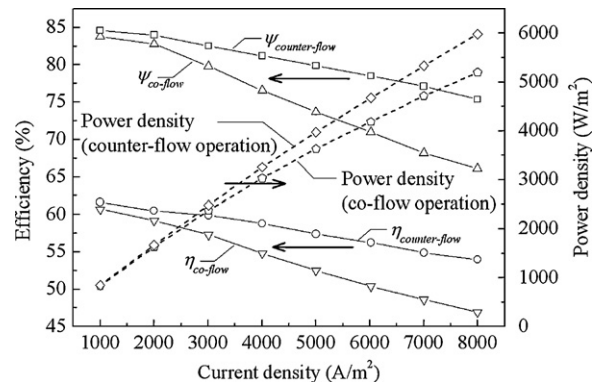Fig. 8. Temperature distributions, counter-flow operation.

Fig. 10. Comparison of efficiencies and power density versus average current density for co- and counter-flow operation.
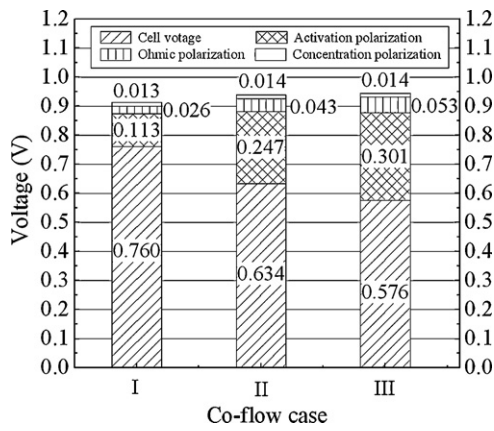
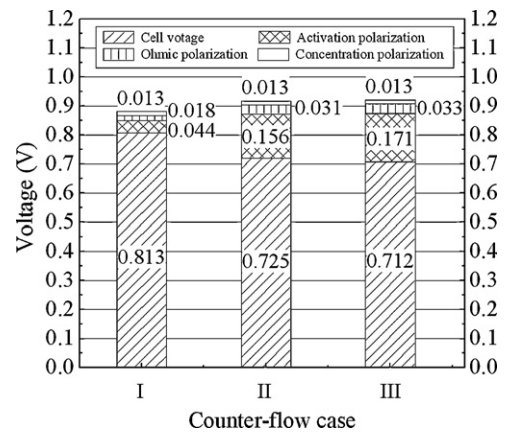Fig. 11. Cell voltage and polarizations, co-flow operation.

Fig. 12. Cell voltage and polarizations, counter-flow operation.

and air utilization factors are kept constant as shown in Table 9, the flow rates are tuned as the average current density is varied. At a high average current density, the flow rates are increased and the amount of heat absorption by the reforming reaction becomes large as well as the heat generation in the cell associated with the electrochemical reaction and other irreversible losses. While the enthalpy of the inlet air flow is immediately supplied to the reforming reaction near the entrance region in the co-flow configuration, the air temperature first increases in the counter-flow configuration accumulating the heat generated in the cell. It results in a difference of the cell temperature, even though the sum of heat generation and absorption in a cell is expected to be similar in the two configurations. The difference of the average cell temperature between two configurations becomes larger as the average current density is increased. Fig. 10 also shows that the energetic and rational efficiencies exhibit similar declining trends. This implies that the increases of the differences between exergy contents of inlet and outlet streams of the cell under co- and counter-flow operations are proportional to the increases of energy in fuel inputs. The decrease of cell performance with increasing the average current density is mainly associated with the increase of the activation polarizations. Fig. 10 and the discussion in the previous sections lead to some considerations: (i) the increase of losses caused by the increased average current density results in the decline of energetic and rational efficiencies; (ii) co-flow operation is favourable for operation at a low current density mode due to the high efficiency and smaller temperature gradient.

The analysis of Fig. 10 shows the advantages of using the present 1-D model in a system analysis. Unlike a lump model that takes only the energy balance into account, the present model considers heat transfer phenomena in the cell and can capture the performance difference caused by the temperature non-uniformity.

3.3. Effects of inlet temperatures

The inlet temperatures of the fuel and air flows are design parameters of a system. It affects the temperature distribution through heat transfer phenomena in the SOFC and eventually affects its performance as explained in the previous sections. A performance comparison was made with co- and counter-flow cell configurations operated at different air and fuel inlet temperature cases as listed in Table 10. Case I is the base case having the inlet fuel and air temperatures shown in Table 9. In Case II, only the inlet air temperature is reduced by 100 K from the base case and kept at 973 K, while both the fuel and air inlet temperatures are set at 973 K in Case III. The average current density is fixed at 4000 A m^{-2} for all cases. The cell terminal voltage and various losses are shown in Figs. 11 and 12, for the co- and counter-flow configurations,

respectively. Although the open circuit voltage increases with decreasing operating temperature, the cell terminal voltage shows the opposite trend accounting of the increase of both ohmic and activation losses. In particular, the increase of the activation polarizations is significant among the three types of losses. The concentration polarizations can be considered as minor importance and are not significantly affected by the inlet temperatures.

The cell temperature distributions of the three cases for the co-flow configuration are shown in Fig. 13. The cell temperature generally decreases when the inlet flow temperature is reduced. The cooling effect of the air temperature is more prominent compared to that of the fuel flow mainly because of its higher flow rate. The distribution profile is generally similar each other but the temperature gradient near the fuel entrance seems to be larger in Case II than other cases. Fig. 14 shows the temperature distributions for the counter-flow configuration. Cooling effects by the reduced inlet temperature are obvious in the figure. As can been seen in Fig. 14, the Case II shows the most uniform temperature distribution among the three cases.

The performance comparison results along with the maximum local cell temperatures ($T_{solid,max}$) and the maximum cell temperature gradients ($\partial T_{solid}/\partial x)_{max}$, well known as the most important operational constraints for the planar SOFC, are listed in Table 10. It shows that the cell performance can be improved by setting the inlet temperatures high because the entire cell is maintained at high temperature as shown in Figs. 11 and 12.

From the view point of a safe operation, cell temperatures (T_{solid}) and cell temperature gradients ($\partial T_{solid}/\partial x$) must be monitored with caution. A steep temperature gradient and high cell temperature can cause a severe adverse effect on the life span of the fuel cell.
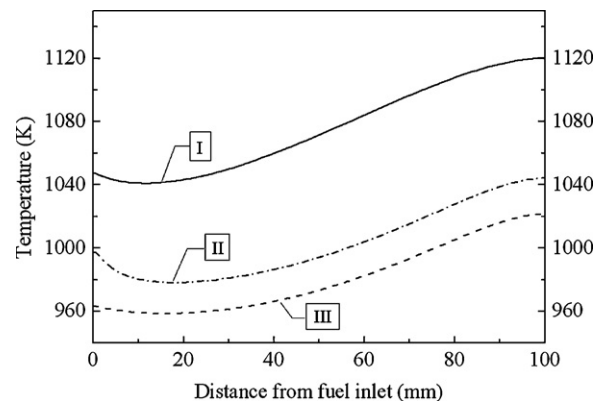

Fig. 13. Comparison of cell temperature distributions based on case studies, co-flow operation.

Table 10
Summary of SOFC performance based on case study.

Inlet stream temp.			Co-flow				Counter-flow			
Case	$T_{fuel,in}$ (K)	$T_{air,in}$ (K)	$T_{solid,max}$ (K)	$(\partial T_{solid}/\partial x)_{max}$ (K mm^{-1})	η	ψ	$T_{solid,max}$ (K)	$(\partial T_{solid}/\partial x)_{max}$ (K mm^{-1})	η	ψ
I	1073	1073	1120	1.28	54.7	76.7	1192	5.17	58.6	81.3
II	1073	973	1044	3.24	45.6	64.0	1077	1.86	52.0	72.8
III	973	973	1021	1.20	41.7	57.6	1071	2.87	51.5	70.5

Table 11
Performance of SOFC with thick anode (anode thickness = 1000 μm).

Inlet stream temp.			Co-flow				Counter-flow			
Case	$T_{fuel,in}$ (K)	$T_{air,in}$ (K)	$T_{solid,max}$ (K)	$(\partial T_{solid}/\partial x)_{max}$ (K mm^{-1})	η	ψ	$T_{solid,max}$ (K)	$(\partial T_{solid}/\partial x)_{max}$ (K mm^{-1})	η	ψ
I	1073	1073	1116	1.23	54.2	75.9	1168	3.39	57.6	79.3
II	1073	973	1041	1.99	45.3	63.4	1062	1.40	51.0	70.8
III	973	973	1017	1.05	41.4	57.0	1052	1.93	49.7	67.7

Their allowable values depend on materials, cell structure and manufacturing process. In this study, the values of the maximum allowable temperature gradient and the maximum allowable cell temperature are set at 1300 K and 5 K mm^{-1} [4], respectively, to consider the viability of SOFC. The maximum local cell temperatures presented in Table 10 do not seem to pose any problem to the cell while the maximum temperature gradient exceeds the allowable criteria in one case.

In case II under co-flow operation, the maximum temperature gradient of 3.24 K mm^{-1} occurs near the fuel entrance, while the efficiencies are between those of the case I and III. While, case I under counter-flow operation is incompatible with the operational constraints. Although case I under counter-flow operation has the highest efficiencies, it is not a preferable operating condition due to the considerably large maximum cell temperature gradient of 5.17 K mm^{-1}, a critical operating condition for the cell. By reducing air stream inlet temperature, case II under counter-flow operation, the maximum cell temperature gradient and maximum local cell temperature are brought down to 1.86 K mm^{-1} and 1077 K, respectively. The study shows that, considering the balance between the cell performance and the operation safety, the most favourable operating condition among the six cases is case I under co-flow operation with the energetic and rational efficiencies of 54.7, and 76.7%, respectively, at moderate maximum cell temperature gradient and moderate maximum local cell temperature of 1.28 K mm^{-1} and 1120 K. For all these results, the performance of DIR-SOFC under co-flow operation has a good potential to be further enhanced by simultaneously increasing inlet fuel and air temperatures until maximum cell temperature and cell temperature gradient approaching the material constraints.

In order to show the importance to consider material constraints more clearly, results of additional simulations of DIR-SOFC with a thick anode are presented. In this simulation, the anode thickness is doubled from its standard size, 500–1000 μm. Other geometric and computational conditions are unchanged from the standard cases discussed above. The performance of the SOFC with thick anode is summarized in Table 11. A comparison with Table 10 shows that the effect of the anode thickness on the energetic and rational efficiencies is minor. The efficiencies of the thick anode cells are 1–2% smaller than those of the standard cells. The drop of efficiency is mainly attributed to the increase of ohmic loss and concentration overpotential. The effect of the anode thickness on the temperature field, on the other hand, is significant. The maximum temperature and temperature gradient are reduced in the thick anode cells compared to those of the standard cells. This is caused by the reduction of the thermal resistance of the cell in the directions parallel to the cell surface. In all calculation listed in Table 11, the maximum temperature and maximum temperature gradient are lower than the allowable limits, 1300 K and 5 K mm^{-1}. Increasing anode thickness allows counter-flow cell configuration to operate within a safe operational condition. In Table 11, considering the balance between the cell performance and the operation safety, the most favourable operating condition among the six cases is case I under counter-flow operation.

The above discussion based on Tables 10 and 11 show that a preferred flow configuration can be changed depending on the cell geometry and operation conditions, if the material constraints are considered. This is a result that can never be obtained if the discussion is based only on the energy efficiency. The energy efficiency of a counter-flow case shown in Tables 10 and 11 is always higher than its counterpart co-flow case.

4. Conclusions

A 1-D numerical model for a planar anode-supported DIR-SOFC with co- and counter-flow configurations was developed and validated. The calculations were carried out varying the average current density (1000–8000 A m^{-2}) and the gas inlet temperatures (973–1073 K) while keeping the fuel and air utilization factors constant at 0.8 and 0.3, respectively. The two configurations were evaluated through energy and exergy concepts with a consideration for the material constraints. Careful attention is paid to the maximum local temperature and the maximum temperature gradient of the cell.
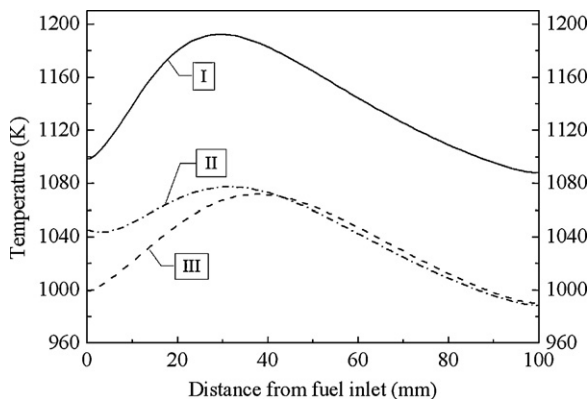
Fig. 14. Comparison of cell temperature distributions based on case studies, counter-flow operation.

1. The significant difference is observed between the rational efficiency and the energetic efficiency in both configurations. It shows potential for additional power generation utilizing the exergy in outlet streams.
2. As the average current density is increased, the efficiencies naturally decrease but the tendency is more prominent in the co-flow configuration. The difference of the efficiencies between the co- and counter-flow configurations is very small at low current density but becomes more pronounced at high current density. The dependency of the energy and rational efficiencies on the flow configurations is successfully captured by applying the 1-D simulation.
3. As a result of the combined effects of heat generation, heat absorption and heat transfer in the cell, non-uniform temperature distribution is formed. The flow configuration affects the convective heat transport and plays a crucial role in supplying heat to the reforming reaction near the fuel entrance. The counter-flow configuration generally achieves high efficiencies but unfavourable in terms of strong temperature gradient. A preferred flow configuration can be changed depending on the cell geometry and operation conditions, if the material constraints are considered.
4. To evaluate the performance of SOFC, the material constraints need to be considered as well as the energy and rational efficiencies. The developed 1-D model based on the energy and exergy concepts can capture the temperature distribution affected by the control parameters of the system, such as the gas inlet temperatures, gas flow rates and the average current density. It is a useful tool for system analysis work to improve the system design and reliability.

Acknowledgements

References

[1] N. Bessette, PhD Thesis 1994, Georgia Institute of Technology.
[2] J. Pålsson, PhD Thesis 2002, Lund University, Sweden.
[3] J. Pålsson, J.B. Hansen, N. Christiansen, S. Nielsen, Proceedings of the Riso International Energy Conference, Denmark, May 19–21, 2003.
[4] C. Stiller, B. Thorud, S. Seljebø, Ø. Mathisen, H. Karoliussen, O. Bolland, J. Power Sources 141 (2005) 227–240.
[5] K.D. Panopoulos, L. Fryda, J. Karl, S. Poulou, E. Kakaras, J. Power Sources 159 (2006) 570–585.
[6] F. Calise, M.D. Accadia, A. Palombo, L. Vanoli, Energy 31 (2006) 3278–3299.
[7] M. Rokni, Energy 35 (2010) 4691–4699.
[8] H. Yoshida, H. Iwai, Thermal Management in Solid Oxide Fuel Cell Systems, Engineering and Technology, Whistler, Canada, 2005, CD-ROM CHE2005-01.1.
[9] A. Sciacovelli, V. Verda, Energy 34 (2009) 850–865.
[10] B.A. Haberman, J.B. Young, Trans. ASME J. Fuel Cell Sci. Technol. (2008) 011006.
[11] F. Arpino, N. Massarotti, Energy 34 (2009) 2033–2041.
[12] H. Iwai, Y. Yamamoto, M. Saito, H. Yoshida, Energy 36 (2010) 2225–2234.
[13] S. Campanari, P. Iora, Fuel Cell 5 (2005) 34–51.
[14] P. Aguiar, C.S. Adjiman, N.P. Brandon, J. Power Sources 138 (2004) 120–136.
[15] M. Li, J.D. Powers, J. Brouwer, ASME J. Fuel Cell 7 (2010) 041017.
[16] T.X. Ho, P. Kosinski, A.C. Hoffmann, A. Vik, Int. J. Hydrogen Energy 34 (2009) 3488–3499.
[17] M.A. Khaleel, Z. Lin, P. Singh, W. Surdoval, D. Collin, J. Power Sources 130 (2004) 136–148.
[18] E. Achenbach, J. Power Sources 49 (1994) 333–348.
[19] M.V. Twigg, Catalyst Handbook, Wolfe Pub. Ltd., London, 1989.
[20] R.H. Perry, Perry's Chemical Engineers' Handbook, 7th ed., McGraw-Hill, New York, 1997.
[21] C.R. Wilke, Diffusional Properties of Multicomponent Gases: Chemical Engineering Progress 46, 1950, pp. 95–104.
[22] F. Zhao, A.V. Virkar, J. Power Sources 141 (2005) 79–95.
[23] Z. Bariza, G.M. Andreadis, M.H. Ben, Int. J. Hydrogen Energy 36 (2011) 4228–4235.
[24] K.J. Daun, S.B. Beale, F. Liu, G.J. Smallwood, J. Power Sources 157 (2006) 302–310.
[25] D.L. Damm, A.G. Federov, J. Power Sources 143 (2005) 158–165.
[26] D.L. Damm, A.G. Federov, J. Fuel Cell Sci. Technol. 4 (2005) 258–262.
[27] J.D.J. VanderSteen, J.G. Pharoah, J. Fuel Cell Sci. Technol. 3 (2006) 62–67.
[28] F.P. Incropera, D.P. Dewitt, Fundamentals of Heat and Mass Transfer, 5th ed., Wiley and Sons Inc., 2002.
[29] S. Nagata, A. Momma, T. Kato, Y. Kasuga, J. Power Sources 101 (2001) 60–71.
[30] T.J. Kotas, The Exergy Method of Thermal Plant Analysis, Reprint ed., Krieger, Florida, 1995.
[31] E. Achenbach, Annex II: Modeling and Evaluation of Advanced Solid Oxide Fuel Cells, Germany, International Energy Agency, 1996.